A PROPANE BURNER TEST FOR PASSIVE FIRE PROTECTION (PFP) FORMULATIONS CONTAINING ADDED HALLOYSITE, CARBON NANOTUBES AND GRAPHENE.

A.G. Gibson[1], W.N.B.Wan-Jusoh[2], G. Kotsikos[1]

[1]Centre for Composite Materials Engineering, Newcastle University,

Newcastle-upon-Tyne NE1 7RU, UK

[2]Universiti Kuala Lumpur (UniKL), Malaysia

Corresponding author email a.g.gibson@ncl.ac.uk

ABSTRACT

Passive fire protection materials (PFP) have been characterised quantitatively using a constant heat flux propane burner test, with the PFP attached to a steel substrate. The burner test was able to produce a large, constant heat flux, to simulate a severe fire condition. The heat transferred through the PFP was calculated from the temperature rise of the steel. A simplified model is discussed, to account for different combinations of substrate thickness, PFP thickness, heat flux and exposure time. It was found that, despite the complex processes of resin decomposition and intumescence, heat transmission could be modelled, to a reasonable approximation, by treating the PFP as a material with single point values of apparent thermal diffusivity and conductivity. This leads to an equation that can be used to characterise PFPs and indeed to specify their required thickness.

The burner test was employed to interpret the effects of adding small quantities of three nano-materials: halloysite nanotubes (HNT), multi-walled carbon nanotubes (MWCNT) and graphene nanoplatelets (GNP), to a standard PFP formulation. It was found that HNT

addition resulted in a significant performance improvement, whereas the other nano-materials did not produce an improvement.

Key words. Propane burner, passive fire protection (PFP), halloysite, multiwall carbon nanotubes (MWCNT), graphene.

Nomenclature

T	(^{0}C)	metal substrate temperature.
T_0	(^{0}C)	initial uniform temperature of the protection layer, the substrate and the environment behind the metal.
T_1	(^{0}C)	hot face temperature of the protection layer.
T_{flame}	(^{0}C)	flame temperature
t	(s)	time.
t_0	(s)	initial time lag.
X	(m)	protection layer thickness.
b	(m)	metal substrate thickness.
ρ_m	(kg.m^{-3})	metal density.
Cp_m	(J.kg^{-1}.K^{-1})	metal specific heat capacity.
k	(W.m^{-1}.K^{-1})	effective thermal conductivity of protection layer.
h	(W.m^{-2}.K^{-1})	heat transfer coefficient at the metal rear surface.
α	(m^{-2}.s^{-1})	effective thermal diffusivity of protection layer.
c		proportionality constant in the time lag relationship.
Q	(J.m^{-2})	cumulative heat flow into metal substrate.

1. INTRODUCTION

Fire protection systems for metallic structures are developed, tested and qualified using constant heat flux tests, involving burning hydrocarbon. The procedures, vary a little between industries. For oil and gas applications, large propane or butane jet-fires are employed, with heat fluxes exceeding 240 kW/m^2 [1, 2]. On the other hand, aircraft-related tests use a smaller-propane or kerosene burner [3] with a heat flux of 116 kW/m^2, and a flame temperature of 1,100 ºC. Recently we developed a simple lab-scale burner test [4,5] with the aim of reducing the cost of materials development. This system, shown in Fig. 1, was used here. A similar approach was recently used by Tranchard *et al.* to study aerospace composites [6] where the procedure was found to be compatible in terms of heat flux with the established test standard [3]. The cone calorimeter [7, 8] has also been used to understand the processes that occur with intumescent PFP systems, but here the heat flux is generally limited by practical considerations to less than 100 kW/m^2.

Figure 1. Propane burner rig employed for the fire exposure tests.

When the temperature of the metal substrate is recorded, different types of PFP display a profile similar to the one in Figure 2. The key features are (i) an initial lag in substrate temperature rise, followed by (ii) a period of rising temperature, then (iii) a progressive decrease in slope. The initial lag is related to the 'effective' thermal diffusivity of the PFP, as well as to any chemical reactions that occur. Endothermic reactions tend to decrease the effective thermal diffusivity, increasing the lag time and *vice versa* for exothermic ones. The behaviour later in the test, which largely determines the temperature reached by the substrate at a particular time, is strongly influenced by the effective long-term thermal conductivity of the charred PFP as well as by cold face heat transfer conditions. Depending on the design of a particular cross-section or structure the cold face heat transfer condition may approximate to 'fully insulated', 'convection to ambient air' or sometimes, in the case of a pipe or tank, convection into the bulk of a fluid.

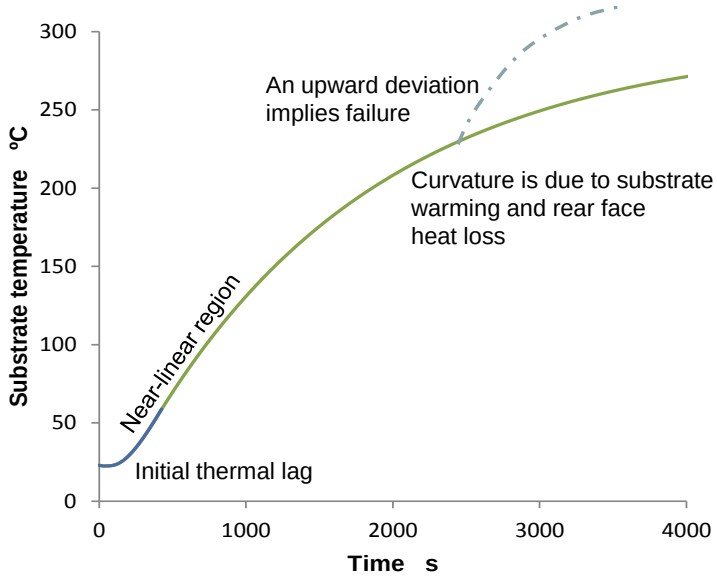

Figure 2. Typical variation of the substrate temperature with time for a fire-protected metal structure in a constant heat flux fire exposure.

Smooth upward or downward deviations from the curve of Figure 1 may be due to reactions such as resin post-cure, gas evolution, intumescence, char development or decomposition. Sudden deviations indicate an event such as fracture, spallation, delamination or debonding of the coating. Most such failure processes result in a sudden upward movement of the line, although delamination of the PFP from the substrate can, in the short term, reduce heat transfer and show the reverse effect. Chemical changes taking place in the coating are most pronounced near to the start of the test, but continue well into the fire exposure period, as a front of decomposition moves through the material.

Although intumescent PFP coatings have been employed for several decades, new interest in improving their formulations and in their broader use, has resulted in several recent reviews [9-14]. In fire, they undergo a series of chemical reactions leading to expansion, and conversion into a stable, low thermal conductivity char. Polymeric intumescents are based on a binder polymer, usually epoxy or acrylic, with three additional active components, whose functions have been well-described in the literature [15-20]. These components are (i) an acid source such as ammonium polyphosphate or one of its derivatives, (ii) a carbon source such as pentaerithritol and (iii) a ‘spumifiant’ or foaming agent, such as melamine, which decomposes to produce further gases which aid expansion.

Our previous work [21] showed that a simple two-parameter model could be applied to both ceramic and organic-based protection systems. The present paper will investigate the model further and explore the extent to which it can be applied to PFPs with nano-additives.

There have been a number of approaches to PFP modelling [7,8,21-28]. The key difficulty is the number of thermal quantities and rate parameters that need to be measured, which effectively limits modelling to a few formulations where the necessary parameters are known. Compounds where the composition is to be varied, as in product development, are problematic. A simple, but realistic model, is therefore attractive.

There is interest, nowadays in the potential for using nano-additives in PFP formulations [29-32]. For instance Isitman and Keynak [30] considered CNTs and nanoclays as possible intumescent synergists for use alongside organophosphorus in PMMA. They noted the importance of effective dispersion of the nano-additives. They found that, although CNTs provided a strong network at the flaming surface the char integrity was actually significantly greater when nanoclays were used. Fina *et al* [31] studied catalytic effects and found that CNTs in polyethylene also promoted a stable surface layer with an oxygen barrier effect. Lecouvet *et al.* [32] showed that HNT had a significant synergistic effect when used alongside APP in polypropylene.

The present paper continues the theme of employing small quantities of nano-additives, using HNT, CNT and GNP in a standard formulation.

2. MODELLING THE SUBSTRATE TEMPERATURE RISE

We assume that there are two stages in the development of a carbonaceous char:

1. An initial 'transient' state, influenced by heat-up of the hot face, the thermal diffusivity of the protection material and the endo- or exo-thermic reactions that take place.
2. A 'steady' region in which the heat flux through the coating is governed by the effective long-term thermal conductivity of the charred protection material.

The hot face achieves a near-constant temperature a short way into the test. This temperature is always significantly lower than the flame temperature, and is influenced by factors such as its absorptivity and the heat conducted into the sample. Here, it was measured using embedded thermocouples and an extrapolation technique, described later. It was assumed to be effectively constant for all the experiments.

The initial thermal lag will be taken as analogous to a thermal diffusivity lag. It is expected that this will be proportional to the square of the thickness of the PFP and inversely proportional to its 'apparent' or 'effective' thermal diffusivity, early in the test, [33,34] so

$$t_0 = cX^2 \cong \frac{X^2}{6\alpha} \tag{1}$$

The relation of this thermal lag to the apparent thermal diffusivity will be discussed later.

In the period following the initial phase it will be assumed that the PFP approximates to a simple thermal resistance, with no thermal energy absorbed or lost. The metal substrate possesses high thermal conductivity, resulting in little temperature variation through its thickness, so the system conforms to the 'lumped parameter' model [33, 34].

Account needs to be taken of convective heat losses from the metal rear face, which can have a significant influence. So, a heat balance can be made: the heat conducted through the PFP, on the left hand side, corresponds to the enthalpy change of the substrate, plus the rear face convective losses, so

$$\frac{(T_1 - T)k}{X} = \frac{dT}{dt}\rho_m C_{Pm} b + (T - T_0)h \tag{2}$$

Re-arranging gives

$$\frac{dT}{T - A} = -\frac{Bdt}{\rho_m C_{Pm} b} \tag{3}$$

The abbreviated terms, A and B are

$$A = \frac{\frac{T_1 k}{X} + T_0 h}{\frac{k}{X} + h} \quad \text{and} \quad B = \frac{k}{X} + h \tag{4}$$

Integrating and applying the boundary condition that the temperature is T_0 at $t = 0$, results in the exponential relationship:

$$T = A + (T_0 - A)\exp\left(-\frac{Bt}{\rho_m C_{Pm} b}\right)$$

(5)

The solution of Equation 5 is shown in Figure (3), where the effect of the heat loss from the rear face of the substrate is seen to be quite significant.

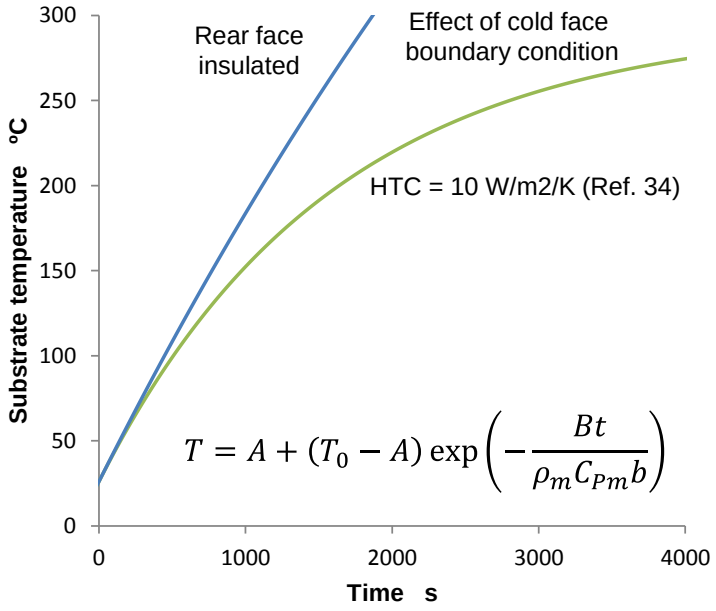

Figure 3. Solution of Equation 5, showing the effect of the substrate cold face heat transfer condition.

The main drawback with the model so far is that it fails to reproduce the initial transient condition and time lag. This can be partially rectified by changing the boundary condition for the integration, so that the temperature is T_0 at $t = t_0$, where the lag time is given by Equation 1, so

$$T = A + (T_0 - A)\exp\left(-\frac{B(t - t_0)}{\rho_m C_{Pm} b}\right) \quad (6)$$

This would produce a horizontal shift to the right in the solutions shown in Figure 3. Equation 6 applies at times significantly beyond the initial transient region. It effectively involves only two unknown parameters that can be determined from test results:

- the thermal lag constant, t_0, which is related to the effective thermal diffusivity, α, and
- the effective long-term thermal conductivity, k, of the PFP.

The fact that Equation (6) does not describe the behaviour early in the test is not a large problem when using it to design thermal protection, because we are mainly interested in behaviour at long times. However, if it should be required to model the temperature early in the test a good approximation can be found from Laplace's equation [33-35]. If the effect of the rising substrate temperature is ignored, so that $(T_1 - T_0)$ is effectively constant, the accumulated heat flow through the PFP, is given by the series solution [33-35]

$$Q = k(T_1 - T_0)\left(\frac{t}{X} - \frac{X}{\alpha}\left(\frac{1}{6} + \frac{2}{\pi^2}\sum_{n=1}^{\infty}\frac{(-1)^n}{n^2}\exp\left(-\frac{n^2\pi^2\alpha t}{X^2}\right)\right)\right) \tag{8}$$

Q is related to the substrate temperature rise by

$$Q = \rho_m C_{Pm} b(T - T_0) \tag{9}$$

so

$$T = T_0 + \frac{k(T_1 - T_0)}{\rho_m C_{Pm} b}\left(\frac{t}{X} - \frac{X}{\alpha}\left(\frac{1}{6} + \frac{2}{\pi^2}\sum_{n=1}^{\infty}\frac{(-1)^n}{n^2}\exp\left(-\frac{n^2\pi^2\alpha t}{X^2}\right)\right)\right)$$

(10)

Again this model involves both the effective thermal diffusivity and the conductivity of the PFP. The solution is shown in Figure 4a. This relationship has not been used widely in the field of heat flow, but its diffusion analogue is often employed in modelling gas permeation through polymer liners [35]. Equation 10 predicts the initial lag in the substrate temperature, which is related to the effective thermal diffusivity by

$$t_0 = \frac{X^2}{6\alpha} \tag{11}$$

so

$$\alpha = \frac{X^2}{6t_0} \tag{12}$$

The thermal lag period is followed by a period of linear temperature increase, in which the maximum slope is determined by the long-term thermal conductivity of the PFP:

$$\frac{dT_0}{dt} = \frac{k(T_1 - T_0)}{\rho C_P b X} \tag{13}$$

Equations 6 and 10 can be combined to model the behaviour over the full temperature range, as shown in Figure 4b. The two curves can be matched in the crossover region by adjusting α to cause the curves to coincide. At longer times, Equation 6 shows a declining slope in contrast to the linear prediction of Equation 10. This is because ($T_1 - T_0$) declines a little with time instead of remaining constant because the metal warms up. The slope is also affected by heat loss from the reverse side of the substrate, as discussed.

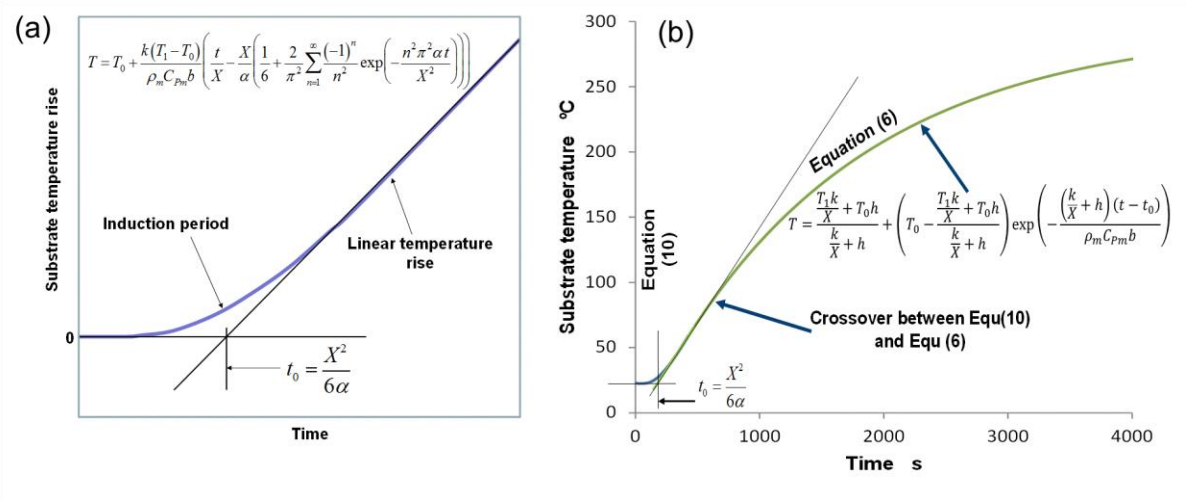

Figure 4. Heat transfer models. (a) Solution of Equation 10. (b) Combination of Equations 6 and 10 to model the full range of times and substrate temperatures.

This simple approach ignores the considerable expansion that occurs as a result of the intumescence, which is 10 times or greater. The value taken for *x* here is simply the original PFP thickness. In considering the long term thermal conductivity of the char, therefore, the actual value will be an order of magnitude larger than the *k* value resulting from Equation 6.

3. EXPERIMENTAL

3.1 Materials and Methods

The materials used for the epoxy-based intumescent coatings are described in Tables 1 and 2. The manufacturers' quoted surface area values for the nano-additives were determined by the BET method [36]. The 'control' PFP formulation, shown in Table 1, employed ammonium polyphosphate (APP), penta-erythritol (PE) and melamine (ME).

Table 1. PFP composition used in the study

Material	Grade	Supplier	Mass %
Epoxy resin	RS-L135	PRF Composite Material	36.87
Epoxy hardener	RS-H137	PRF Composite Material	13.13
Ammonium polyphosphate (APP)	Exolit AP422	Clariant Produkte Germany	25
Pentaerythritol (PE)	P4755	Sigma Aldrich UK	12.5
Melamine (ME)	M2659	Sigma Aldrich UK	12.5

Table 2. Nano-additives, with manufacturers' characterisation data.

Material	Grade and description	Supplier	BET surface area Ref. [36]
Halloysite nanotubes (HNT)	Silicate nanotubes Diameter: 30-70 nm Length: 1-3 µm	Sigma Aldrich UK	64 m^2 g^{-1}
Multi-wall carbon nanotubes (MWCNT)	NC7000 Diameter ~9.5 nm Length: ~1.5 µm	Nanocyl	250-300 m^2 g^{-1}
Graphene nanoplatelets (GNP)	Grade C XGnP 1-50 µm diameter platelets	XG Sciences Inc. USA	500 m^2 g^{-1}

In addition to the control formulation, the intention was to prepare modified intumescent systems containing 0.5 wt.% and 5 wt.% of the nano-fillers described in Table 2, added to the baseline formulation. The three nano-additives employed were halloysite silicate nanotubes (HNT), multiwall carbon nanotubes (MWCNT) and graphene nanoplatelets (GNP). These were incorporated as additions to the baseline formulation. They were first dispersed in the epoxy resin using a staged mixing process, in a polyethylene mixing vessel, with a mechanical mixer and an ultrasonic disperser. First, a 1.1 kW Klarstein laboratory mechanical mixer, with a single 'z'-shape mixing paddle, was used at a speed to 2,000 rpm. This operation was alternated with three 3-minute periods of sonication using a Heilscher UP200S 200 W, 24 kHz, ultrasonic disperser on its highest setting. Following this, the resin was mixed with the hardener using the Klarstein mixer and finally the APP/PE/ME powder components were mixed together and added, before casting the PFP onto the metal substrates.

All but one of the intended formulations were successfully made: the 5 wt.% MWCNT formulation was unsuccessful due to the high viscosity of the mix, and the difficulty of dispersing the additive at this level. This produced a very lumpy viscous compound that could not be easily handled or cast.

The metal substrate was in the form of 150 mm square, 10 mm thick steel plates, cleaned and degreased using acetone, then allowed to dry before applying a 5 mm thick layer of the intumescent coating. The coatings were applied to the steel plates immediately after mixing. Although no cure characterization was performed, the coatings were all observed to be solid and firm to the touch after 24 hours. In line with industry practice, no post-curing heat treatment was carried out since, with field-applied PFP, this is not practical. The samples were kept at room temperature for 7 days before the fire exposure tests.

3.2 Burner Test

The experimental arrangement, Figure 1, employed a 63.5 mm diameter 'Bullfinch No. 1270' propane burner, placed at 350 mm from the sample hot face. This type of entrainment mixing burner has been used previously for tests on composite materials in our research group [4,5] and also by Tranchard *et al*. [6]. The propane pressure was adjusted to ensure that the burning gas temperature 10 mm in front of the sample hot face, was 1,000 ºC, corresponding to a heat flux of 100 kW/m^2, using the heat flux calibration procedure described previously [4,5]. It was necessary to angle the burner slightly downwards from horizontal to compensate for the buoyancy of the flame and to ensure that the hottest region of the flame impacted the centre of the specimen. Before commencing each run, an inert sample of calcium silicate board was placed at the sample location and used to determine the required gas pressure, after which the board was replaced by the sample. It was found that the 1,000 ºC condition in the hot gas was maintained during the test with little or no further adjustment of the gas pressure. The temperature fluctuation of the hot face thermocouple during the test, due to flame

turbulence was just ±15 ^{0}C. One of the advantages claimed for this type of burner [4,5] is that the burning volatiles resulting from the sample decomposition are swept rapidly away from the sample surface, reducing their effects on the sample hot face temperature. Recently the gases evolved with epoxy composites, and their effects, have been discussed in some detail by Tranchard *et al.* [6]

The cold face temperature of each sample was measured by a thermocouple bonded, with epoxy adhesive, into a 5 mm deep hole, drilled in the steel.

3.3 Hot face temperature measurement

The PFP hot face temperature was measured by embedding thermocouples at depths of 2 mm and 4 mm in the surface of samples having the 'control' formulation, as shown in Figure 5. This was accomplished by milling slots of the appropriate depth in the surface, placing the thermocouples, then filling the remaining slot space with the same control PFP composition and allowing to cure. The thermocouple wires were led out of the side face of the sample. The temperatures were recorded during the fire exposure test and the surface temperature was then estimated by extrapolation. Of course the samples intumesced during fire exposure, so the thermocouple depths were no longer 2 mm and 4 mm. However, it was assumed that, after a period of time, with steady temperatures reached at both thermocouples, the thermal properties and expansion of the PFP would be roughly uniform up to the location of the deeper thermocouple. Figure 5 shows typical thermocouple traces, along with the linearly extrapolated hot face temperature for the control sample. The temperature at a depth of 4 mm was found to be constant after 300

seconds. These measurements were carried out on five control samples and the average hot face temperature was found to be 684±10 ºC. This is, of course, substantially lower than the measured temperature in the burning flame near to the hot face, reflecting the combined effects of the flame emissivity and the absorptivity of the hot face. The hot face temperature measurements were only carried out for the control composition, it being assumed that the values for the other samples would be similar.

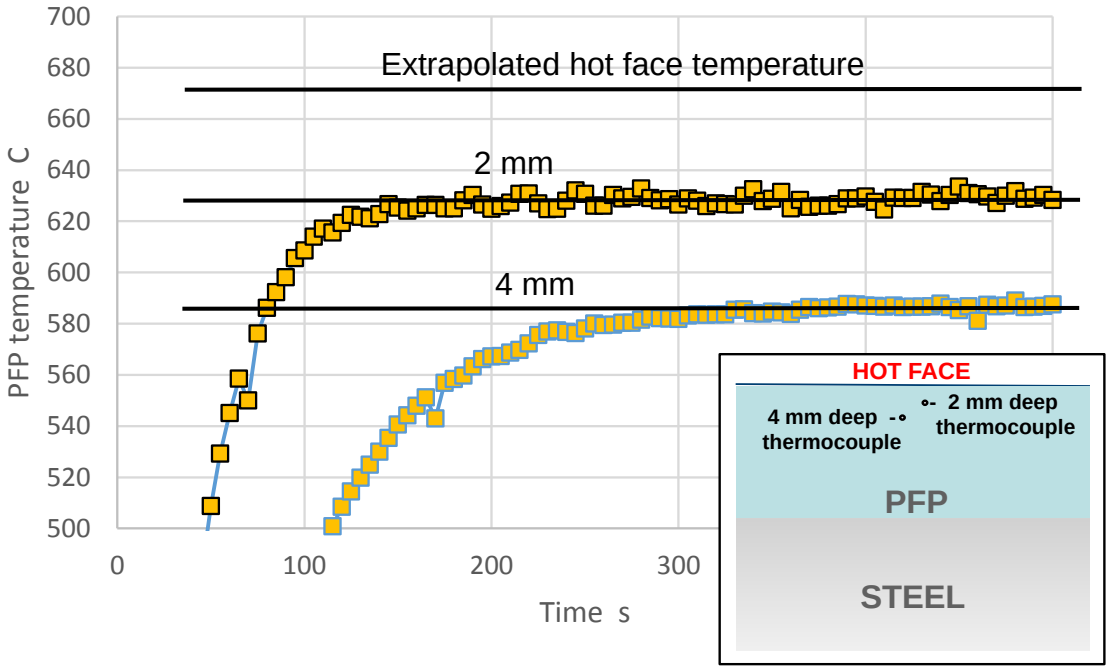

Figure 5. Hot face temperature measurement procedure.

4. RESULTS AND DISCUSSION

Figure 6 shows the steel temperature for the control sample, along with the relationship predicted by Equation 6. The two parameters needed to fit the curves: the lag time, t_0, and the apparent thermal conductivity, k, of the established char were determined as described below. A cold face heat transfer coeefficient, h, of 10W/m^2/ºC, was chosen,

which is typical for a vertical steel surface in ambient air[33]. The fitting of the model curve was achieved by adjusting the two key parameters as follows:

(i) The value of t_0 was adjusted so that the model curve agreed with the experimental curve at 40 °C, i.e. in the region immediately following the thermal lag.

(ii) The thermal conductivity value, k, was then adjusted to achieve agreement over a region of results, some way into the test period.

This procedure converged after two iterations. It was found, with the control results in Figure 6, that there was good agreement between the curves over the range 2,500-4,000 s, after which the experimental curve deviated upwards.

With all the results reported here there was a similar region of agreement between model and experiment. However, it is relevant to note that the agreement between experiment and model is not as good here as we observed in our prevous paper [21], which involved different PFP systems. Nevertheless, it was possible with the present results to make inferences about the behaviour in regions where the model disagreed with the experiment.

In general, it was found, as in Figure 6, that there was an initial region where the experimental temperature was higher than the modelled one, attributable to exothermic reactions occurring during APP decomposition, intumescence and char formation. Then there was good agreement for a period, after which the experimental curves deviated upwards a little from the modelled ones, the inference being that the thermal conductivity

of the char is increasing above the value used to fit Equation 6, probably implying some deterioratiion of the char. The final region of increasing slope for the experimental curve suggests incipient failure of the coating. In the control case, the char layer showed numerous cracks and fissues after the test was stopped at 7,000 s. The maximum thickness of the char was approximately 10 times that of the original PFP layer.

Table 3 shows the values of the thermal lag, the apparent thermal conductivity (from Equation 6) and values of thermal conductivity used to fit all of the experimantal results.

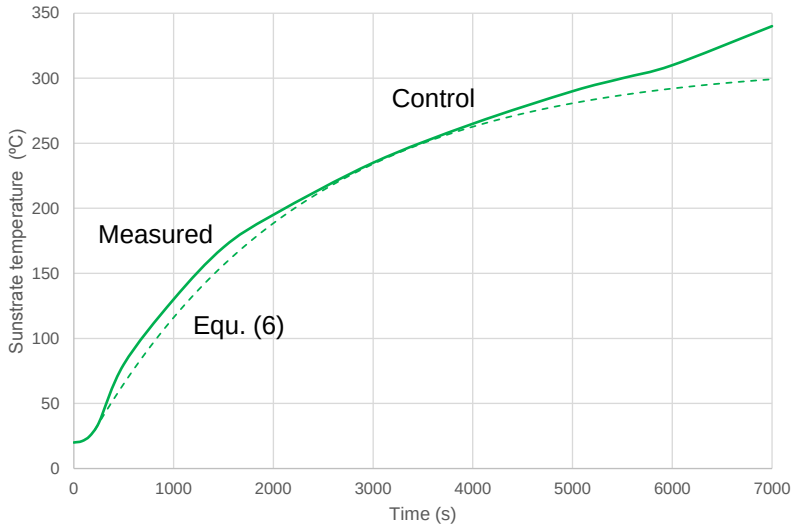

Figure 6. Substrate temperature rise for the control intumescent system, measured results (continuous curve) and modelled values with Equation 6 (dashed curve).

4.1 Halloysite addition

Figure 7 shows a comparison between the control sample and the formulations with 0.5wt% and 5wt% of added HNT. The HNT samples followed the control sample closely,

up to about 1,600s, at which time there is a reduction in the rate of temperature rise, suggesting an improvement in the structure of the char. Both the HNT samples showed significantly better behaviour than the control, the optimum addition being closer to 0.5% than 5%. This effect, where the lower concentration is more effective, is not unusual when adding nanomaterials to composite samples. It is probably associated with clumping, due to van der Waals attraction, and the resulting difficulty of dispersing the nanomaterial effectively at the higher concentrations.

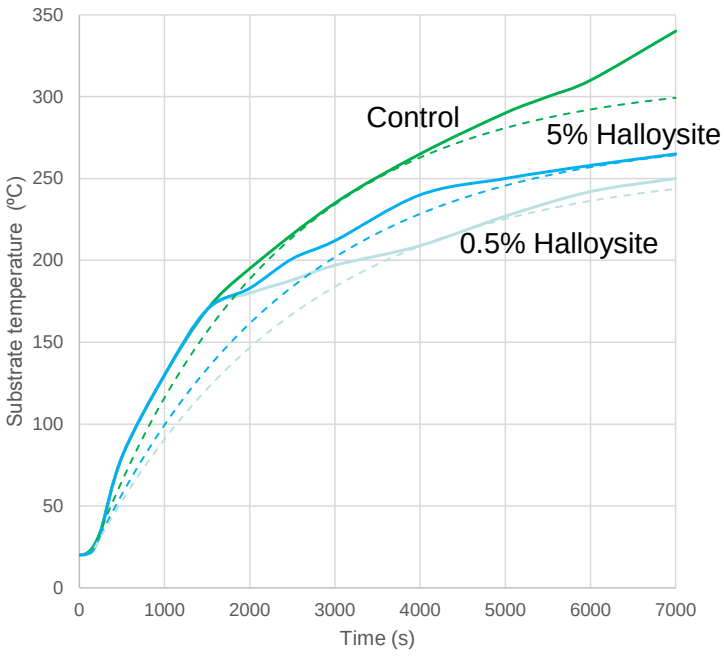

Figure 7. Comparision of the substrate temperature rise for the control intumescent system (green) and the compositions with 0.5 wt% (grey) and 5 wt% of HNT (blue). Measured values (continuous curves); modelled values (dashed curves).

The beneficial effect of HNT may be due to a number of factors, including the well-known catalytic properties of this high surface area nanotubular material which could have the effect of accelerating any or all of the stages in intumescent char formation: the

APP decomposition, the dehydrogenation of the PE and/or the epoxy resin, and also the char development. The nanotubes themselves could also play a role in improving the integrity of the char by reinforcement or crack-bridging. In addition, HNT evolves a small amount of water due to the dehydroxylation that takes place around 500 ºC, which is also beneficial.

Some clues to the effect of HNT can be seen from the SEMs in Figure 8, which show the surface of the residual char from the control sample and the one with 0.5wt% HNT. The control sample, Figure 8a, shows an undulating char structure, in which strings of either voids or small particle residues from the intumescence can be seen.

The HNT sample, Figure 8b, shows a more coherent char structure, with the clear presence of fan-like structures. The nanotubes appear to have unwrapped, fanned out and spread to the surface during the intumescence process. The size of the fan-shaped entities is roughly the same as the initial length dimension of the nanotubes. The presence of a relatively large proportion of the fan structure at the surface is probably the result of the expansion, stretching and gas flow that occurs during intumescence. It is also possible that the fans may be preferentially alinged on the surface due to surface tension. This 'skin' may have several beneficial effects, including reduction of gas loss and the provision of a shielding layer of lower emissivity and lower permeability to oxygen.

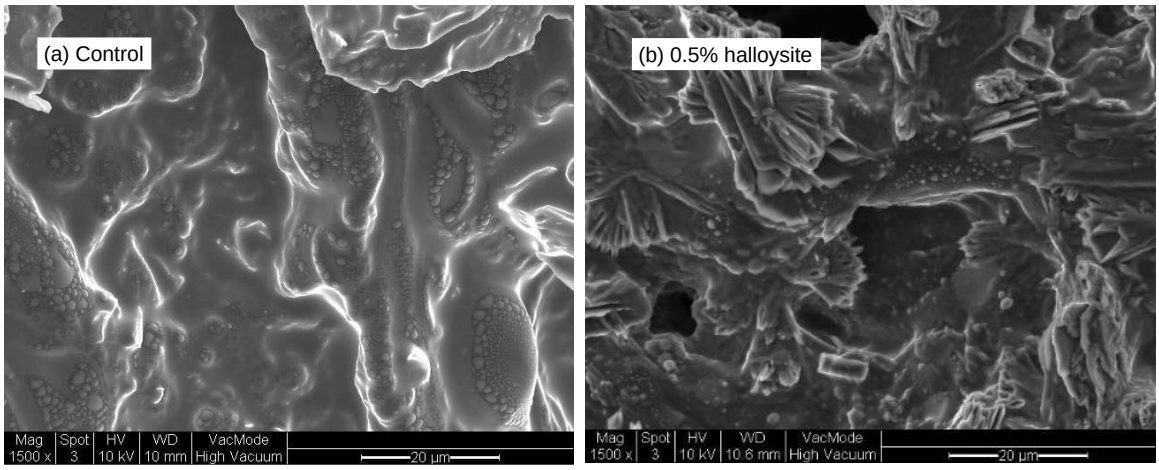

Figure 8. SEM images of the char developed in (a) the control composition and (b) the sample with 0.5 wt% HNT.

There has been debate about why halloysite, which has a silicate lamellar structure similar to kaolin, should exist in the curled up 'scroll' form in nature. The consensus is that this is due to the adsorption of various species, including water, on the silicate surface, which causes a through-thickness strain imbalance, which is accommodated through curvature and eventual complete rolling up of the lamellae to form the spiral structures, with water or other molecules in the gallery between the layers [37]. It appears that the scrolls may be induced to wrap or unwrap depending on temperature and the surrounding environment. In the present case this is likely to be influenced primarily by water and phosphoric acid from the APP decomposition. The transition from scroll to exfoliated lamella offers the interesting possibility of maintaining the halloysite in nanotube form during mixing and application of the PFP, where it has the smallest effect on viscosity and where it is protected from breakage. This is followed, in the fire-induced intumescence, by the transition to unwrapped fan-like lamellae which are most effective in reinforcing the char structure, forming a shielding layer and acting as a

catalyst to the intumescence reactions. Such an unwrapping process would lead to an order of magnitude surface area increase, which would increase the value for the halloysite (Table 2) from 64 m^2g^{-1} up to a value comparable to the values for MWCNT and GNP. The formation of fan shapes, rather than flat lamellae could be accounted for by unwrapping occuring to a different extent along the length of the nanotube scroll, due, possibly to variations in the local composition and acidic environment.

4.2 MWCNT addition

Figure 9 shows the effect of adding of MWCNT to the control formulation. In contrast to the HNT this significantly diminishes the performance of the PFP. The MWCNT response curve deviates upwards from the control from about 500 s onwards, indicating inferior behaviour. Beyond 3,000 s the MWCNT curve turns upwards with increasing slope, suggesting incipient failure. The test was terminated after 4,770 s, at which time the PFP was observed to have begun to break away.

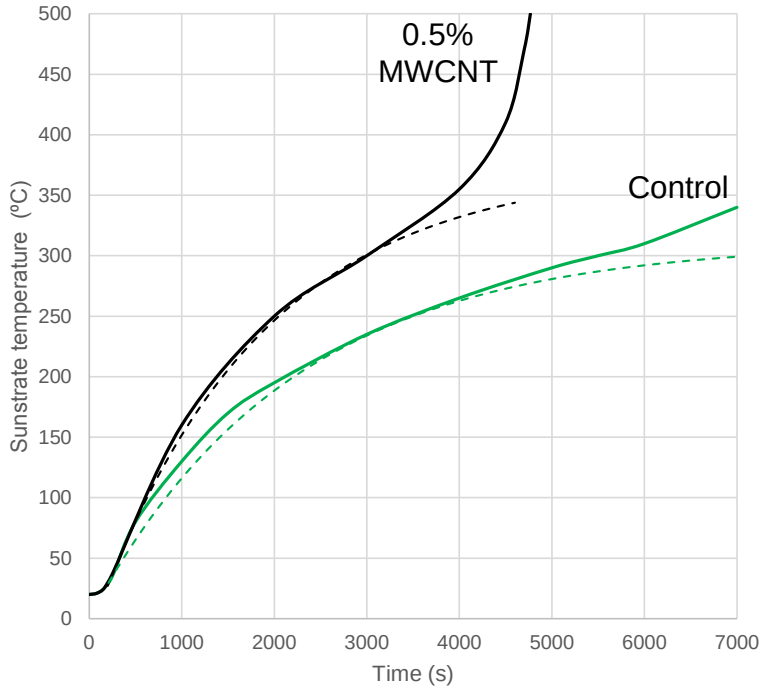

Figure 9. Comparision of the substrate temperature rise for the control intumescent system (green) and the composition with 0.5 wt% of MWCNT (black). Measured values (continuous curves); modelled values (dashed curves).

4.3 Graphene addition

Figure 10 shows the effect of adding 0.5 wt% and 5 wt% of GNP to the control formulation. As with MWCNT the GNP curves deviate upwards, initially, from the control from about 500 s onwards, suggesting inferior behaviour. The 5 wt% GNP curve showed an increasing upward slope, with failure of the coating being approached after 6,400 s, when the test was terminated. The char that formed was significantly inferior to that of the control, showing a number of surface cracks during the test. By contrast, the 0.5 wt% GNP curve, which initially followed the 5 wt% curve, began to show significant improvement later in the test, with a decline in slope commencing at about 1,600 s. This suggested that the char structure began a progressive improvement. By the end of the test the 0.5 wt% GNP temperature was similar to and ultimately slightly lower than the control.

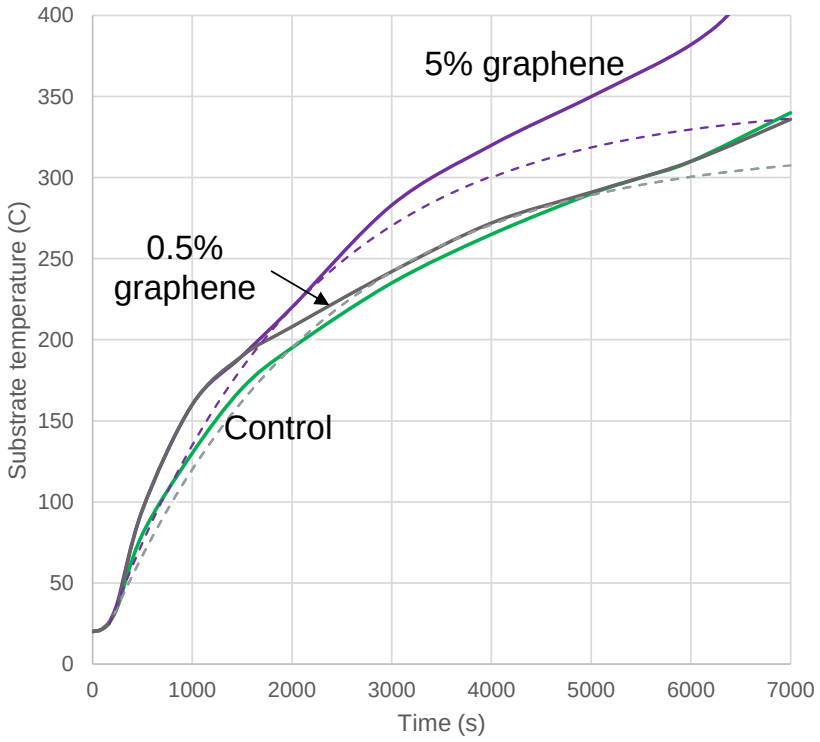

Figure 10. Comparision of the substrate temperature rise for the control intumescent system (green) and the compositions with 0.5 wt% (black) and 5 wt% (purple) of GNP. Measured values (continuous curves); modelled values (dashed curves).

Figure 11 shows SEM images of the char structure in the case of the 0.5 wt% MWCNT and 0.5 wt% GNP samples. The MWCNT sample, Figure 11a, shows many nodules, approximately 10 microns in size, which were probably associated with undispersed nanotube clumps. As mentioned, the MWCNT was the most difficult nano-additive to disperse in the epoxy resin formulation- to the extent that the paste prior to casting possessed a notable nodular structure. It is probable that the smaller diameter and higher aspect ratio of the MWCNTs, Table 1, compared to the halloysite ones, along with their considerably higher surface area, resulted in a much more pronounced tendency to form

these clumps, which affected the processability of the paste. MWCNT is known to have catalytic effects on char formation when effectively dispersed in synergistic flame retartants(). In the present case, however, beneficial catalytic effects seem to have been absent, probably due to the clumping of the nano-particles.

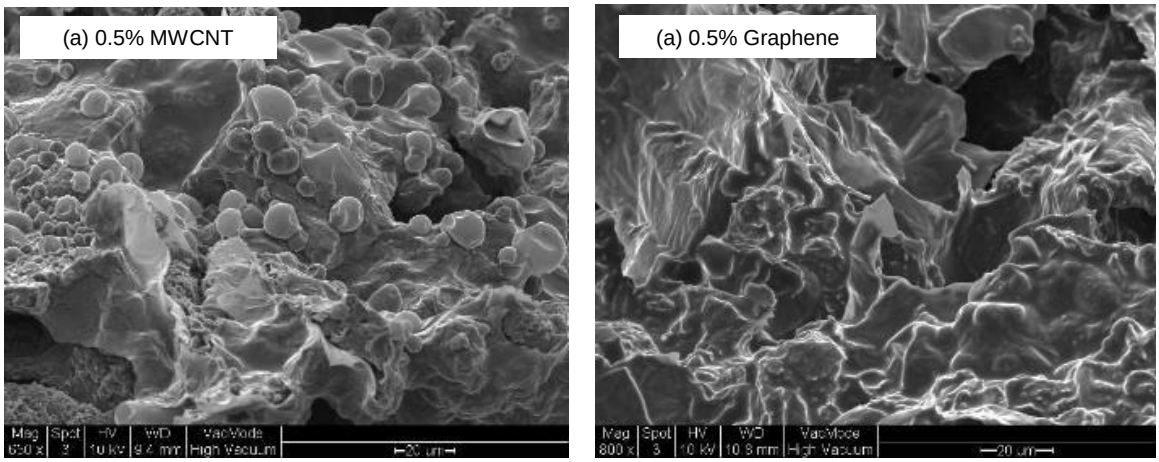

Figure 11. SEM images of the char developed in (a) the sample with 0.5 wt% MWCNT and (b) the sample with 0.5 wt% GNP.

By contrast, Figure 11b shows that the presence of GNP produces a smoother char, with no nodules and rounded corners to all surface features. This may account for the better performance of GNP as an additive, compared to MWCNT. The downward deviation in substrate temperature rise that commences about 1,500 s into the test suggests that the GNP promotes a reduction in thermal conductivity suggesting an improvement in integrity of the char. This is also possibly a catalystic effect due, in part, to the large surface area of the GNP plates. There may also be an effective physical contribution from the GNP in terms of reinforcing the walls of the cells in the char structure as well as acting as a barrier surface layer in a similar way to the halloysite.

Both the MWCNT and GNP samples may have been at a disadvantage, compared to the control and HNT samples, because of their black pigmentation. However this would only have applied early in the tests, as the control and HNT samples also quickly blackened on decomposition.

It is interesting to look at the apparent values, in Table 3, of thermal properties used to fit the modelled curves. The effective *k* values are informative, as they correlate with the behaviour in the tests- the best performing materials, the HNT compound and the Control having the lowest values. The range of apparent values, 0.13-0.16 $Wm^{-1}K^{-1}$, is intermediate between the values for polymer foams and solid polymers at room temperature. It also compares well to mineral wool insulation, where *k* varies from 0.03-10 $Wm^{-1}K^{-1}$ in the range from 20-1,000 ºC. The α values, at 0.1-0.18 $mm^2\ s^{-1}$, are similar to those for polymer resins and do not correlate especially to properties. This underlines the importance of the effective thermal conductivity in determining PFP performance.

Table 3: Apparent thermal data from Equations 6 and 10.

Sample	**Measured protection layer thickness** t (mm)	**Delay time** t_o (s)	**Apparent Thermal Diffusivity** α Equation 12 ($mm^2\ s^{-1}$)	**Apparent Thermal Conductivity** k (**W** $m^{-1}\ K^{-1}$)
Control sample	11	137	0.15	0.086
Control plus 0.5 wt.% HNT	10	133	0.13	0.056
Control plus 5% wt.% HNT	11	136	0.15	0.07
Control plus 0.5 wt.% MWCNT	10	163	0.10	0.114
Control plus 0.5 wt.% GNP	10	141	0.12	0.082
Control plus 5 wt.% GNP	12	133	0.18	0.116

5. CONCLUSIONS

Measuring the metal substrate temperature is an effective means of characterising the performance of PFP materials. The two-parameter thermal model proposed here for the substrate temperature works well and provides useful guidance on whether the PFP is improving or deteriorating during the test. The model also offers a possible method of designing the coating thickness needed for a particular substrate thickness, heat flux and maximum substrate temperature.

In the present study the burner test procedure could be used to distinguish and interpret the changes in the performance of a PFP formulation when small quantities of halloysite, MWCNT and GNP were added. Halloysite showed a significant effect in improving the effectiveness of the PFP in minimising heat flow into the substrate, which was attributed to catalytic effects and the formation of a shielding layer. The halloysite nanotubes were

found to unwrap on heating to form 2-dimensional fan-like structures. GNP did not produce any overall improvement but did show some evidence of shielding layer formation. MWCNT proved difficult to disperse in the PFP and somewhat diminished its effectiveness due to the preence of undispersed clumps. With both MWCNT and GNP thene there may have been some negative effects due to increased thermal conductivity and the increased absorptivity of the char surface.

Acknowledgements

W.N.B. Wan-Jusoh wises to acknowledge Universiti Kuala Lumpur (UniKL) for supporting her PhD studies.

Declaration of Interests: None.

REFERENCES

1. Jet Fire Test Working Group, "Large Scale and Medium Scale Jet Fire Tests" UK HSE, Offshore Technology Report OTO 97 079, 1998.
2. ISO 22899-2:2103 Determination of the resistance to jet fires of passive fire protection -- Part 2: Guidance on classification and implementation methods
3. ISO2685:1998(E). Aircraft-environment test procedures for airborne equipment – resistance to fire in designated fire zones.
4. AG Gibson, ME Otheguy Torres, TNA Browne, S Feih, AP Mouritz, High temperature and fire behaviour of continuous glass fibre/polypropylene laminates. Composites A. 2010 41 (9) 1219-1231.
5. Gibson AG, Browne TNA, Feih S, AP Mouritz. Modelling composite high temperature behaviour and fire response under load. J Compos Mater 2012; 46: 2005–2022.
6. Tranchard P, Samyn F, Duquesne S, Thomas M, Estebe B, Montes M-L, Bourbigot S, Fire behaviour of carbon fibre epoxy composites for aircraft: novel test bench and experimental study, J. of Fire Sci, 2014; 33(3): 247-266.
7. Bartholmai M and Schartel B. Assessing the performance of intumescent coatings using bench-scaled cone calorimeter and finite difference simulations. Fire Mater 2007; 31: 187–205.
8. Bartholmai M, Schriever R and Schartel B. Influence of external heat flux and coating thickness on the thermal insulation properties of two different intumescent coatings using cone calorimeter and numerical analysis. Fire Mater 2003; 27: 151–162.

9. Weil ED. Fire-protective and flame-retardant coatings- a state-of-the-art review. J Fire Sci 2011; 29: 259–295.
10. Alongi J, Han Z, Bourbigot S. Intumescence: tradition versus novelty. A comprehensive review. Prog Polym Sci 2015; 51: 28–73.
11. Vandersall HJ. Intumescent coating systems: their development and chemistry. J. Fire and Flamm, 1971; 2: 97-140.
12. Mariappan T, Recent developments of intumescent fire protection coating for structural steel: a review. J. of Fire Sciences (2016) 34(2) 120–163. DOI:10.1177/0734904115626720.
13. Bourbigot S, Bras ML, Duquesne S, et al. Recent advances for intumescent polymers. Macromol Mater Eng 2004; 289: 499–511.
14. Bourbigot S and Duquesne S. Fire retardant polymers: recent developments and opportunities. J Mater Chem 2007; 17: 2283–2300.
15. Camino G, Costa L, Trossarelli L. Study of the mechanics of intumescence in fire retardant polymers: Part 1- Thermal degradation of ammonium polyphosphate-pentaerythritol mixtures. Polym Degrad Stabil 1984; 6: 243–252.
16. Camino G, Costa L, Trossarelli L. Study of the mechanism of intumescence in fire retardant polymers: Part III- Effect of urea on the ammonium polyphosphate-pentaerythritol system. Polym Degrad Stabil 1984; 7: 221–229.
17. Camino G, Costa L, Trossarelli L. Study of the mechanism of intumescence in fire retardant polymers: Part IV- Evidence of ester formation in ammonium polyphosphate-pentaerythritol mixtures. Polym Degrad Stabil 1984; 8: 13–22.
18. Camino G, Costa L, Trossarelli L. Study of the mechanism of intumescence in fire retardant polymers: Part V- mechanism of formation of gaseous products in the thermal degradation of ammonium polyphosphate. Polym Degrad Stabil 1985; 12: 203–211.
19. Jimenez M, Duquesne S, Bourbigot S. Multiscale experimental approach for developing high-performance intumescent coatings. Ind & Eng Chem Res 2006; 45: 4500–4508.
20. Jimenez M, Bellayer S, Naik A, Bachelet P, Duquesne S, Bourbigot S. Topcoats versus durability of an intumescent coatings. Ind & Eng Chem Res 2016; 55 (36): 9625.
21. Gibson AG, Kotsikos G, DiModica P, Christke S, Wan Jusoh W, Yi K, Mouritz AP, Kandare E, Model for the Characterisation and Design of Passive Fire Protection (PFP) Systems for Steel Structures, 17th Eur. Conf. on Composite Materials (ECCM17), Munich, 26-30 June 2016.
22. Mouritz AP, Feih S, Kandare E, Gibson AG, Thermal-mechanical modelling of laminates with fire protective coating. Comp B, 2013; 48: 68-7811.
23. Kandare E, Griffin GJ, Feih S, Gibson AG, Lattimer BY, Mouritz AP. Fire structural modelling of fibre-polymer laminates protected with an intumescent coating. Comp A, 2012; 43: 793-802.
24. Zhang C, Usmani A.. Heat transfer principles in thermal calculation of structures in fire, Fire Safety Journal, (2015) 78 85-95. http://dx.doi.org/10.1016/j.firesaf.2015.08.006
25. Zhang Y, Wang YC, Bailey CG, Taylor AP, Global modelling of fire protection performance of an intumescent coating under different furnace fire conditions, J. Fire Sci.31(1)(2012)51–72.

26. Zhang Y, Wang YC, Bailey CG, Taylor AP, Global modelling of fire protection performance of intumescent coating under different cone calorimeter heating conditions, Fire Saf. J.50 (2012)51–62.
27. DiBlasi C, Branca C, Mathematical model for the non-steady decomposition of intumescent coatings, AIChE J. 47 (10) (2001) 2359–2370.
28. Gomez-Mares M, Tugnoli A, Landucci G, Cozzani V, Performance Assessment of Passive Fire Protection Materials, Ind. Eng. Chem. Res., 2012, 51 (22), 7679–7689.
29. Proc., Int. Conf. on Nanostructured materials and their use in fire retardancy applications, KTH Stockholm, 23-24 November 2016.
30. Isitman NA, Keynak C, Nanoclay and carbon nanotubes as potential synergists of an organophosphorus flame-retardant in poly(methyl methacrylate). Polym. Deg. and Stab. (2010) 95 9 1523-1532.
31. Fina A, Bocchini S, Camino G, Catalytic fire retardant nanocomposites. Polymer Degradation and Stability (2008) 93 9 1647-1655.
32. Lecouvet B, Sclavons M, Bailly C, Bourbigot S, A comprehensive study of the synergistic flame retardant mechanisms of halloysite in intumescent polypropylene. Polymer Degradation and Stability (2013) 98 2268-2281.
33. Crank J, The Mathematics of Diffusion, Clarendon Press, Oxford, 2nd Edition. 1975.
34. Incropera FP, Lavine AS, Bergman TL, DeWitt DP, Fundamentals of Heat and Mass Transfer, 7th Edition, John Wiley and Sons, Hoboken NJ, 2011. ISBN 13 978-0470-50197-9.
35. Flaconnèche B, Klopffer M-H, Martin J, Oil & Gas Sci and Techn, 2001; (56): 261-278.
36. Brunauer S, Emmett PH, Teller E. Adsorption of Gases in Multimolecular Layers, J of the Amer Chem Soc, 1938; **60** (2): 309–319. ISSN 0002 7863.doi:10.1021/ja01269a023.
37. Singh B, Why does halloysite roll? –a new model. Clays and Clay Minerals (1996) 44 2 191-196.